

CO₂ breakthrough—Caprock sealing efficiency and integrity for carbon geological storage

D. Nicolas Espinoza^{a,*}, J. Carlos Santamarina^b

^a Department of Petroleum and Geosystems Engineering, The University of Texas at Austin, Austin, TX, USA

^b Earth Science and Engineering, King Abdullah University of Science and Technology, Thuwal, Saudi Arabia



ARTICLE INFO

Keywords:

Percolation
Drainage
Non-miscible fluid displacement
Sealing capacity
CCS
Relative permeability

ABSTRACT

Small pores in high specific surface clay-rich caprocks give rise to high capillary entry pressures and high viscous drag that hinder the migration of buoyant carbon dioxide CO₂. We measured the breakthrough pressure and ensuing CO₂ permeability through sediment plugs prepared with sand, silt, kaolinite and smectite, and monitored their volumetric deformation using high-pressure oedometer cells. The data show water expulsion and volumetric contraction prior to CO₂ breakthrough, followed by preferential CO₂ flow thereafter. Our experimental results and data gathered from previous studies highlight the inverse relationship between breakthrough pressure and pore size, as anticipated by Laplace's equation. In terms of macro-scale parameters, the breakthrough pressure increases as the sediment specific surface increases and the porosity decreases. The breakthrough pressure is usually lower than the values predicted with average pore size estimations; it can reach ~6.2 MPa in argillaceous formations, and 11.2 MPa in evaporites. The CO₂ permeability after breakthrough is significantly lower than the absolute permeability, but it may increase in time due to water displacement and desiccation. Leakage will be advection-controlled once percolation takes place at most storage sites currently being considered. Diffusive and advective CO₂ leaks through non-fractured caprocks will be minor and will not compromise the storage capacity at CO₂ injection sites. The “sealing number” and the “stability number” combine the initial fluid pressure, the buoyant pressure caused by the CO₂ plume, the capillary breakthrough pressure of the caprock, and the stress conditions at the reservoir depth; these two numbers provide a rapid assessment of potential storage sites. Unexpected CO₂ migration patterns emerge due to the inherent spatial variability and structural discontinuities in geological formations; sites with redundant seal layers should be sought for the safe and long-term storage of CO₂.

1. Introduction

Carbon geological storage can help mitigate the emission of anthropogenic carbon dioxide CO₂ to the atmosphere (Pacala and Socolow, 2004; IPCC, 2005; Benson and Cole, 2008; Consoli et al., 2015). Most carbon storage target sites considered to date involve high permeability rocks and unconsolidated sands as CO₂ repositories, overlaid by a low permeability caprock formation that serves as a seal. Although the gas and oil industry has the technology required to inject CO₂ underground, cost and knowledge gaps prevent the decisive adoption of carbon geological storage worldwide. Some of the knowledge gaps relate to long-term trapping mechanisms, chemo-hydro-mechanical couplings and emergent phenomena, induced seismicity, and reliable leak estimation and monitoring.

CO₂ is lighter than water at pressure and temperature conditions found at most target formations. CO₂ buoyancy creates a pressure

difference at the seal $\Delta P = (\rho_w - \rho_{CO_2})gh$ that is proportional to the CO₂ plume height h and the difference in mass density $\rho_{CO_2} - \rho_w$, where the mass density of CO₂ ρ_{CO_2} depends on in-situ pressure and temperature conditions (Fig. 1a). The shape of the CO₂ plume depends on the reservoir physical and geometric properties (e.g., entry value, permeability, layering, heterogeneity and spatial correlation, anisotropy, and dipping); injection rate and pressure affect the plume characteristics near the wellbore (e.g., capillary/viscous fingering and fracturing) (Chang et al., 1994; Zhou et al., 2010; Jung et al., 2017). The dissolution of CO₂ into brine and the ensuing density-driven convective-flow carry CO₂ away from the CO₂ plume (Kneafsey and Pruess, 2010). The injection pressure at the bottom-hole must exceed the in situ fluid pressure but it must remain below the fracture stress gradient. Excess fluid pressure builds up in the reservoir during injection unless water-extraction wells operate concurrently with CO₂ injection (Bergmo et al., 2011; Ehlig-Economides and Economides, 2010). The

* Corresponding author.

E-mail address: espinoza@austin.utexas.edu (D.N. Espinoza).

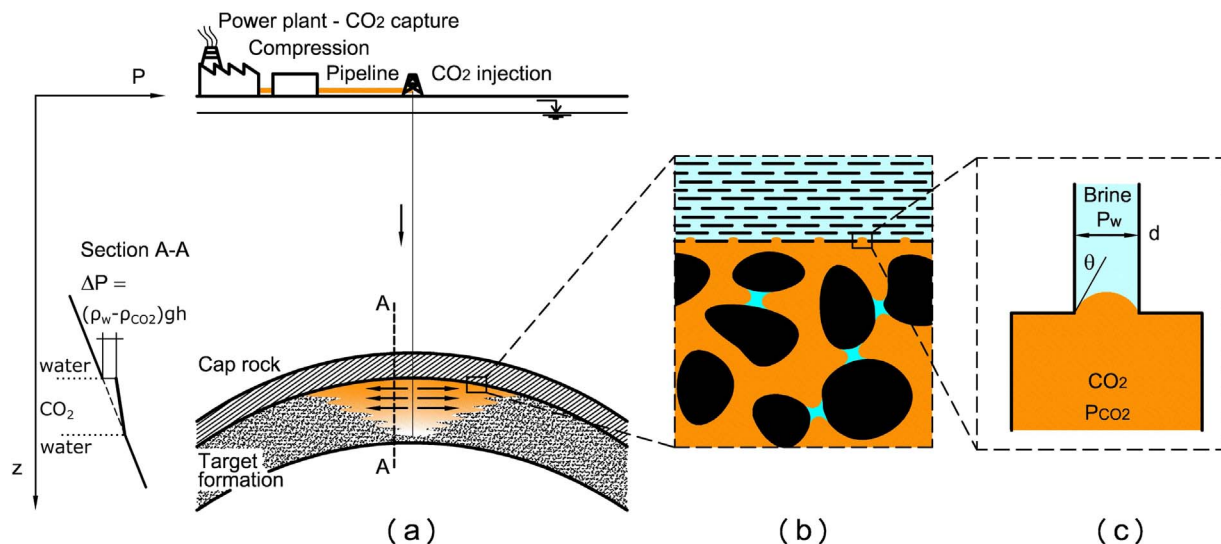


Fig. 1. Carbon geological storage. (a) A fossil fuel plant equipped with CO₂ capture technology and CO₂ delivery to the injection point within a deep permeable geological formation beneath a caprock. (b) CO₂-water capillary menisci at the interface between the repository and the caprock trap the buoyant CO₂. (c) Capillary tube analogy for water-wet minerals.

excess pressure dissipates in time as CO₂ dissolves in water, however, the buoyancy induced pressure remains.

The caprock must resist the short-term excess injection pressure, and the long-term buoyancy pressure. Ductility allows it to deform without developing high permeability pathways (Downey, 1984; De Paola et al., 2009). A good seal layer is continuous and prevents CO₂ transport: a leak rate of 3 kg/m²/yr corresponds to ~2 cm of the CO₂ pool height, and it is enough to saturate the pore water in a shallow 100 m sediment column in 100 years (typical porosity of 0.4). Furthermore, the CO₂-saturated surface water may acidify up to pH = 3.5 and trigger extensive mineral dissolution (Kim and Santamarina, 2014). Clearly, faults, fractures, and abandoned wellbores are preferential paths for CO₂ leakage (Chiodini et al., 1995; Rutqvist, 2012; Wigley et al., 2012; Cartwright and Santamarina, 2015).

Capillary and viscous forces hinder flow through the “intact” caprock (Fig. 1). Consequently, the low viscosity of CO₂ and the low water-CO₂ interfacial tension enhance the risk of leaks. The development of a percolating CO₂ phase, and ensuing caprock permeability determine the post-breakthrough CO₂ transport (Fleury et al., 2010; Gherardi et al., 2007). The caprock spatial heterogeneity defines the path of least resistance for CO₂ leaks (Cavanagh and Haszeldine, 2014; Meckel et al., 2015). Besides advection, CO₂ may be transported by diffusion through the intact caprock. In the absence of large permeability features, the diffusive front does not exceed 10 m in 1000 years and may be further limited by redox reactions and carbonate precipitation (Gaus et al., 2005; Rohmer et al., 2016; Kampman et al., 2016).

The caprock sealing capacity may degrade in time due to: (1) hydraulic fracture and fault reactivation by reservoir overpressure (Rutqvist and Tsang, 2002; Chiaramonte et al., 2008; Rinaldi and Rutqvist, 2013), (2) aqueous CO₂ diffusion into caprock water (without bulk CO₂ invasion) and consequent water acidification and mineral dissolution (Berne et al., 2010; Gaus et al., 2005; Gherardi et al., 2007; Yoksoulian et al., 2013); and (3) CO₂ invasion into the caprock, capillary breakthrough, and CO₂ advection (Angeli et al., 2009; Hildenbrand et al., 2004; Li et al., 2005; Wollenweber et al., 2010). For example, extensive mineral dissolution and precipitation has been reported at natural CO₂ reservoirs (Allis et al., 2001; Watson et al., 2004; Wigley et al., 2012), and evidence of remineralization has been observed at CO₂ enhanced oil recovery sites (Emberley et al., 2004; Gunter et al., 2000; Kaszuba et al., 2005). Other less known coupled processes include: (1) reactivity of water dissolved in CO₂ (McGrail et al., 2009; Choens et al., 2016), (2) CO₂ intercalation in clays (Schaef et al., 2012;

Heller and Zoback, 2014; Busch et al., 2016), (3) changes in electrical interaction between clay particles due to water acidification and displacement by CO₂, and (4) caprock dehydration and capillary-driven volumetric contraction (Espinoza and Santamarina, 2012).

The objectives of this study are to analyze the transport of CO₂ through well-characterized reconstituted sediment samples as analogues of mudrocks, and to estimate potential leak rates through caprocks at CO₂ storage sites. The manuscript documents a CO₂ pressure breakthrough experimental study involving various water/brine saturated sediments. Finally, we use data from the literature and experimentally validated analytical models to anticipate reservoir scale implications in the presence of structurally sound and homogeneous caprocks. These assumptions allow us to estimate an upper-bound for the sealing capacity of caprocks.

2. Fundamental concepts and physical properties

2.1. CO₂-water properties

The physical properties of CO₂ depend on pressure and temperature conditions. The CO₂ mass density ρ_{CO_2} varies from ~500 kg/m³ to 800 kg/m³ within potential reservoir pressure-temperature ranges (Span and Wagner, 1996). Other pressure-temperature dependent properties of CO₂ include the bulk compressibility (typically an order of magnitude higher than that of water), and viscosity (about 5–10 times lower than water, $\mu_{CO_2} \sim 50 \times 10^{-6}$ Pa s at 20 MPa and 360 K (Fenghour et al., 1998)). CO₂ is electrically non-conductive (Tanaka et al., 2008). The buoyant pressure developed by the CO₂ plume is directly proportional to the difference between brine and CO₂ mass density. The magnitude of CO₂ leaks after breakthrough is inversely proportional to CO₂ viscosity.

The water-CO₂ interfacial tension is pressure-temperature dependent, as well. It decreases from $T_s \sim 72$ to 25 mN/m as the pressure increases from 0.1 MPa to 6.4 MPa at ~298 K, and eventually plateaus at $T_s = 25 \pm 5$ mN/m when CO₂ is in supercritical state (Kvamme et al., 2007). High salinity levels can increase the water-CO₂ interfacial tension by 10 mN/m (Espinoza and Santamarina, 2010). The contact angle formed by the CO₂-water interface on mineral surfaces varies according to the solid wettability: about $\theta \sim 40^\circ$ on water-wet amorphous silica and calcite surfaces, $\theta \sim 50^\circ$ to 120° on coal, $\theta \sim 40^\circ$ to 60° on mica, $\theta \sim 85^\circ$ to 95° on oil-wet amorphous silica, and 8° to 30° on organic shale surfaces (angle measured through the water phase in all cases – Chi et al., 1988; Chiquet et al., 2007; Chalbaud et al., 2009;

Espinoza and Santamarina, 2010; Iglesias et al., 2015; Guilletin et al., 2017). The breakthrough pressure is directly proportional to the interfacial tension and the cosine of the contact angle. The interfacial tension of water-CO₂ systems is lower than those in CH₄-water and oil-water systems (Ren et al., 2000; Peters, 2012). Experimental evidence shows changes of CO₂ wettability with pressurization and surface alteration particularly in oil-wet and organic-rich mineral surfaces (Chiquet et al., 2007; Espinoza and Santamarina, 2010; Guilletin et al., 2017).

CO₂ dissolves in water to form aqueous carbon dioxide. The solubility of CO₂ in water x_{CO_2} [mol/L] satisfies Henry's law $x_{CO_2} = k_H \varphi P_{CO_2}$, where the Henry's coefficient k_H is a temperature dependent variable ($k_H \approx 0.035 \text{ mol(gas)}/[\text{L(water)} \text{ atm}]$ at 25 °C) and the fugacity coefficient φ ranges from 1 at low pressure to ~0.1 at supercritical conditions (Stumm and Morgan, 1996). The solubility of CO₂ in water ranges from $x_{CO_2} \approx 1$ to 2 mol/L at reservoir pressures between $P = 10$ and 50 MPa, and temperatures in the range of $T = 25\text{--}150$ °C relevant to potential storage sites (Spycher et al., 2003). CO₂ dissolution in water favors solubility trapping but acidifies water and may induce dissolution and precipitation of minerals with ensuing changes in caprock stresses and petrophysical properties.

2.2. Caprocks

Mudrocks and evaporites are common seals found above hydrocarbon reservoirs. Clays are fundamental building blocks in mudrocks, such as shales and mudstones (Gueguen and Palciauskas, 1994). Table 1 summarizes petrophysical properties of shales and evaporites at selected carbon storage sites. Burial depth, effective stress-driven mechanical compaction, chemical diagenesis, and cementation reduce the porosity and the pore size of mudrocks (Nygard et al., 2004). Porosity decreases exponentially with effective stress, and constitutive parameters correlate with the sediment specific surface S_s (Burland, 1990; Santamarina et al., 2001; Chong and Santamarina, 2016). The porosity of shales ranges from ~1% to 12%, the mean pore size from 5 nm to 100 nm, and the permeability from 10^{-21} m^2 to 10^{-19} m^2 (Katsube and Williamson, 1994; Watson et al., 2005; Armitage et al., 2010). The following section reviews the key physical properties that affect the sealing capacity of caprocks (Note: we do not address caprock reactivity and ensuing changes).

2.3. Hydro-chemo-mechanical phenomena in CO₂-water-mineral systems

2.3.1. Breakthrough pressure

The capillary breakthrough pressure $P_c^* = P_{CO_2} - P_w$ for a water-CO₂ interface in a porous medium is a function of the interfacial tension T_s between water and CO₂, the contact angle θ formed by the water-CO₂ interface on the mineral surface, and the minimum pore size d^* along a percolating path across the medium,

$$P_c^* = \frac{\psi T_s \cos \theta}{d^*} \quad \text{Laplace's equation} \quad (1)$$

where the ψ -factor reflects pore shape, $\psi = 4$ for tubes and $\psi = 2$ for parallel plates. The solution for a percolating breakthrough path in a porous medium with uniform pore size yields d^* equal to the pore size diameter. However, most sediments exhibit a log-normal pore size distribution with mean $\mu = \text{mean}[\log(d/\text{nm})]$ and standard deviation $\sigma^2 = \text{variance}[\log(d/\text{nm})]$, where σ is often proportional to the μ (Phadnis and Santamarina, 2011). Thus, the characteristic pore size d^* of a percolating breakthrough path can be related to the mean μ by a factor α of the standard deviation σ , such that $\log(d^*/\text{nm}) = \mu + \alpha \sigma$. Experimental data indicates that breakthrough in homogeneous media happens along pores larger than the mean pore size (Espinoza and Santamarina, 2010). Some rocks and fine-grained sediments may exhibit a dual or triple porosity with dominant pore sizes at various length scales, and laminations parallel to bedding (Lloret et al., 2003; Peters,

2012). Table 2 summarizes previous breakthrough studies in shales, marl, evaporites, and limestone conducted with He, N₂, CO₂, and CH₄. The measured CO₂ breakthrough pressures are less than ~6.2 MPa in mudrocks and less than ~11.2 MPa in evaporite rocks. These breakthrough measurements suggest that percolating paths connect pores larger than > 15 nm in mudrocks and > 9 nm in evaporites.

2.3.2. Electrical forces

Caprocks are brine saturated. Clay-forming caprocks react to changes in the surrounding pore fluid. The surface charge of clay particles is pH-dependent: low pH promotes protonation, leading to positively charged surfaces (Lyklema, 1995; Stumm and Morgan, 1996; Santamarina et al., 2001). Hydrated ions are attracted to charged clay surfaces, form a diffuse counter-ion cloud, and give rise to electrostatic repulsion among contiguous particles. As opposed to water, CO₂ is a non-polar, low permittivity fluid. Hence, a change in the electrical equilibrium of the forces acting on clay particles is expected as CO₂ enters the pore space; implications include: a reduction in osmotic repulsion, dissolution of residual water in CO₂ and salt precipitation, and a three-fold increase in the Hamaker constant for clay-CO₂-clay as compared to clay-water-clay (Espinoza and Santamarina, 2012). Changes in electrical forces can induce clay swelling or shrinkage, and stresses changes in the caprock.

2.3.3. Suction and volumetric changes

The mechanical properties of fine-grained sediments are sensitive to water saturation and associated suction (capillary pressure), leading to phenomena such as swelling during wetting, and volumetric contraction and even desiccation cracks during drying (Sánchez et al., 2005; Shin and Santamarina, 2010; Espinoza and Santamarina, 2012). An increase in suction Δs produces a decrease in void ratio $\Delta e = -(\kappa_s/s)\Delta s$, proportional to the sediment compressibility κ_s (Alonso et al., 1990). The tendency to volumetric contraction is magnified in high specific surface clays like montmorillonite. Capillarity-induced volumetric contraction causes stresses changes, particularly in the more compressible caprocks.

2.3.4. Relative permeability and residual saturation

The sediment absolute permeability, water saturation, and viscosity control the advective transport of CO₂ after breakthrough (Pentland et al., 2011). The relative permeability of CO₂ in mudrocks depends on the pore structure and the capillary pressure, and it is proportional to CO₂ saturation (Bachu and Bennion, 2008). For typical percolating saturations $S_{CO_2} < 0.3$, the Corey-Brook equation predicts a relative permeability $k_{rCO_2} < 0.3^2 = 0.09$ (Peters, 2012). Further CO₂ invasion reduces the remaining water saturation and increases the CO₂ relative permeability. The uncertainty in CO₂ permeability values determines the uncertainty in potential leaks estimates.

3. Device, materials, and experimental procedure

3.1. Device

The spring-loaded high-pressure oedometer designed for this study applies a constant vertical effective stress up to $\sigma_z' = 3$ MPa, equivalent to about 300 m of burial from surface, and can withstand a pore-fluid pressure $P = 20$ MPa (Fig. 2). A radial fluid pressure gradient is imposed from the periphery towards the drainage tube at the center of the specimen. This design minimizes leaks between the specimen and chamber walls in standard rigid-wall one-dimensional permeameters. The specimen diameter is $d_c = 40$ mm and its height $h \sim 35$ mm; the collection pipe diameter is $d_p = 3.17$ mm. We measure and/or control: (1) the inlet CO₂ pressure P_{in} [MPa] = P_{CO_2} in the CO₂ reservoir, (2) the exit pressure downstream P_{out} [MPa], (3) the amount of water displaced during CO₂ invasion m_w [m³], (4) the flow rate of CO₂ through the specimen q_{CO_2} [kg/s], and (5) the vertical displacement on the

Table 1
Petrophysical and geometrical properties of caprocks at selected carbon storage sites. Most seal layers are shales, evaporites or a layered sequence of the two.

Site	Reservoir	Caprock			Porosity	Pore size distribution	Permeability	Breakthrough pressure CO ₂	References
		Depth	Thickness	Pressure					
Frio, USA	1450 m	12 m	15.4 MPa	75 m	Illite-smectite ~45%, illite ~10%, Kaolinite 13%, Chlorite ~3% Calcite (trace)	8–10%	—	1.7 MPa*	Hovorka (2009); Lynch (1997); Sakurai et al. (2006)
SACROC, USA	2000 m	150 m	16.6 MPa	150 m	62% Illite-smectite, Calcite 2.5%, Dolomite 2%, 0.1% Halite	1.3%	—	< 50 nD \perp to bedding	—
Krechba, Algeria	1850 m	20 m	17.9 MPa	950 m	Muscovite-Illite ~25–50%, Chlorite ~20–40%, Kaolinite ~8–4%, Siderite ~15–0%	1.8–11.3%	Mean ~5–236 nm (low porosity layers)	—	Garey et al. (2007); Han et al. (2010); Amitige et al. (2010); Mathieson et al. (2010)
Sleipner, Norway	250 m (water) + 750 m	250 m	10.3 MPa	100 m	Mica-Illite ~25%, Kaolinite 14–18%, Smectite 3–9%, Chlorite 1–4%, Calcite 1–3%, Siderite 2%	35%	45–55% particles < 2 μ m	—	Boe and Zweigle (2001); Chadwick et al. (2004); Pillitteri et al. (2003); Tonnet et al. (2011)
Rousse, France	400 m	400 m	4 MPa	2000 m	Illite 2.2–14.5%, Kaolinite 0.3–4.1%, Chlorite 0.1–2%, Calcite 30–65%, Dolomite 3–63%, Siderite 0.1–6.2%	0.5–3%	Primary: 1–100 μ m Secondary: d ~ 10 nm Bodies: < 500 nm	< 1 nD at $\sigma' > 10$ MPa 2.25–3 MPa [†] and > 7.6 MPa	2.25–3 MPa [†] and > 7.6 MPa
Ketzin, Germany	600 m	20 m	7.5 MPa	85 m	Illite 42–74%, Chlorite 1–3%, Dolomite 4–35%, Halite (small fraction)	10%	31.8 nD–< 10 nD	0.54–3.89 MPa [†]	Förster et al. (2007); Kiessling et al. (2010); Boulin et al. (2013)
Otway, Australia	1980 m	—	—	—	Kaolinite 44–17%, Illite 6–1%, Smectite 3–1%, Siderite 35–2%	~2.5–7.5%	Throats: 10–36 nm	—	1–2 MPa*
Carnarvon, Australia	1100 m	—	—	—	Illite-smectite 30–25%, Illite 15–20%, Kaolinite 15%, Chlorite 5% – Siderite 1–40%	21%	Mean ~17 nm	—	3–4 MPa*
Weyburn, Canada	3800 m	—	—	—	Mostly anhydrite – Dolomite traces	0.2–0.5%	40% < 2 μ m	6–25 nD	5–11.2 MPa
									Li et al. (2005)

Notes: *capillary threshold pressure converted from mercury (T_s , Hg-air = 0.485 N/m) to CO₂ (T_{scCO_2} -water = 0.025 N/m).

[†]converted from nitrogen (T_s , N₂-brine = 0.057 N/m) to CO₂ (T_{scCO_2} -water = 0.025 N/m).

Table 2

Previous gas-breakthrough experimental studies.

Medium	Fluid	CO ₂ breakthrough pressure [MPa]	Permeability [10^{-21} m^2]	Reference
Bentonite blocks	He	2.6–6.25 [†]	5–30	Horseman et al. (1999)
Claystone and mudstone	N ₂	0.03–2.9 [†]	3–550	Hildenbrand et al. (2002)
Shale, marl, limestone, and sandrock	CO ₂ , CH ₄ and N ₂	0.1–4.9	< 1–89	Hildenbrand et al. (2004)
Limestone and clay rich marl	CO ₂ and He	limestone: 0.74 marl: ~0.5	limestone: ~0.5 marl: ~3	Wollenweber et al. (2010)
Evaporite	CO ₂ , CH ₄ and N ₂	5–11.2 and > 21 (N ₂)	6–70	Li et al. (2005)
Marl	CO ₂ and N ₂	> 7.6	< 1–20	Tonnet et al. (2010, 2011)
Shale	CO ₂	3.5–4	60	Angeli et al. (2009)
Limestone	N ₂	0.37–1.82 [†]	1070–1680	Boulin et al. (2013)
Mudstone/Anhydrite	N ₂	0.54–3.89 [†]	14.5–31.8	Boulin et al. (2013)
Opalinus clay	CO ₂	2.8–4.6 (resedimented) 1.6 (intact)	9 (resedimented) 5 (intact)	Makhnenko et al. (2017)

Note: [†]Converted from nitrogen ($T_{sN2\text{-water}} = 0.057 \text{ N/m}$) or Helium ($T_{sHe\text{-water}} = 0.068 \text{ N/m}$), to CO₂ ($T_{sCO2\text{-water}} = 0.025 \text{ N/m}$).

specimen top surface Δz [m]. The transparent high-pressure chamber connected to the exit port is used to observe CO₂ breakthrough – bubbles – and to measure CO₂ flow rate.

3.2. Materials

We prepared homogeneous specimens made of fine sand F110 (U.S. Silica), precipitated calcium carbonate PCC (Imerys Carbonates), crushed calcium carbonate CCC (Huber Enginnered Materials), kaolinite SA1 and RP2 (Wilkinson Kaolin Co.), and bentonite (PureGold GEL, Cetco). Specimens were mixed with either deionized water or brine (2 mol NaCl per kg of water). The CO₂ is research-grade (Airgas). Table 3 summarizes the parametric study and materials involved in all tests.

3.3. Procedure

The selected sediment slurries are statically compacted to reach an effective stress of $\sigma'_z \sim 0.4 \text{ MPa}$, then trimmed to fit the high-pressure oedometer. A layer of filter paper sits between the specimen and the

oedometer wall to facilitate CO₂ entry from the peripheral boundary. Grease seals the lower and upper pistons to prevent transport through these interfaces (non-reactive with CO₂ – Goop, Swagelok). Once in the oedometer, the specimen is spring-loaded gradually to reach an effective stress of $\sigma'_z = 2 \text{ MPa}$. After consolidation, we increase the inlet pressure P_{in} to cause CO₂ radial invasion into the sediment; the outlet pressure remains constant at $P_{out} = 0.1 \text{ MPa}$ throughout the test. Each injection-pressurization cycle includes a holding period when the inlet valve remains closed and the inlet pressure P_{in} is recorded in time. Monitoring continues until vertical displacement Δz and the volume of displaced water m_w approach asymptotic values. Eventually, CO₂ breaks-through and CO₂ flow rate q_{CO2} is monitored thereafter.

Test completion and disassembly involved four steps: (1) slow fluid decompression allowing for equilibration, (2) spring load removal, (3) specimen recovery, and (4) forensic visual inspection.

4. Results and analyses

A total of 16 experiments were completed for this study. This section presents a typical time-response first, followed by a compilation

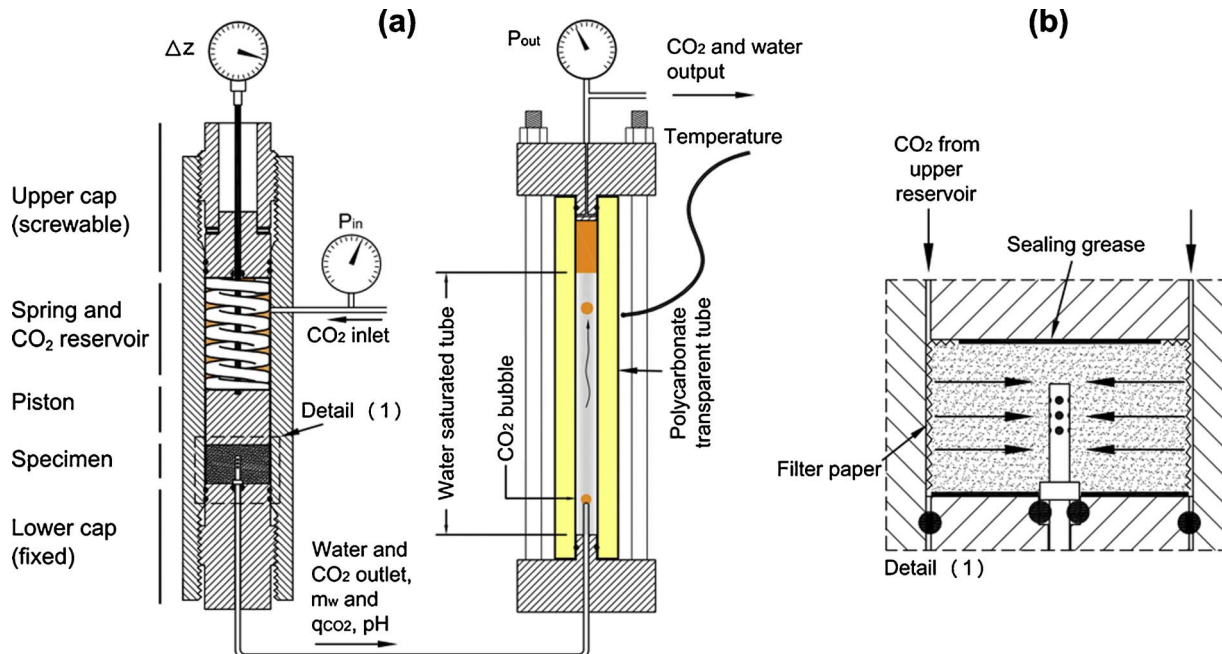


Fig. 2. Experimental device. (a) Specimens are compacted under zero lateral strain boundary conditions. The space above the piston hosts a CO₂ “reservoir” and a heavy-load spring that is used to apply the vertical effective stress to the sediment. The transparent high-pressure chamber on the right reveals CO₂ breakthrough and flow rate. Pressure transducers, displacement gauges, and pipettes are used to measure pressure P_{in} , P_{out} , settlement Δz , displaced water m_w , and CO₂ flow rate q_{CO2} . (b) Detail of the sediment plug and boundary conditions.

Table 3

Summary of sediments used in this study, physical properties, and experimental results. CO₂ is in gas condition in all experiments except in Kaolinite clay RP2 experiment during flushing post breakthrough. All experiments run at controlled laboratory temperature 23 ± 1 °C.

Sediment	Specific surface* S_s [m ² /g]	Mineral density ρ_m [kg/m ³]	Mean grain size D_{50} [μm]	Saturating pore fluid	Breakthrough Pressure [MPa]	Void ratio at breakthrough e	Water (absolute) permeability [10 ⁻²¹ m ²]	Klinkenberg correction coefficient** b [MPa]	CO ₂ permeability after breakthrough [10 ⁻²¹ m ²]	CO ₂ permeability during CO ₂ flush [10 ⁻²¹ m ²]	Final water saturation
Sand F110	0.02	2650	110	Deionized water	~0.0045	0.80	1.8 × 10 ⁹	–	–	–	–
					0.0043–0.0069	0.80	1.8 × 10 ⁹	–	–	–	–
					–	0.82	1.6 × 10 ⁹	0.0025	2.39 × 10 ⁶	–	–
					–	0.89	2.1 × 10 ⁹	0.0025	8.36 × 10 ⁶	–	–
CCC	1.98	2700	12	Deionized water	0.11–0.29	0.64	9600	0.3	15.9–32.5	275	0.940
PCC	10	2710	1	Deionized water	0.53–1.09	1.2	787	0.4	21.6–45.1	–	0.804
Kaolinite clay SA1	13	2600	1.1	Deionized water	1.283–2.46	–	340	0.4	6–142	147	0.753
					1.47–2.7	0.63	–	0.4	8–51	955	0.619
					0.81–1.21	0.63	1100	0.4	12–52	365	0.7568
					0.85–1.1	0.59	–	0.4	57–4	156	0.920
Kaolinite clay RP2	21.9	2600	0.36	Brine 2M	1.8–2.8	0.73	1510	0.4	1–9	1730 (liquid CO ₂)	0.486
Montmorillonite clay	320	2500	–	Brine 2M	0.85–2.6	0.695	86	2.0	9–1	140	0.824
					1.06–2.4	0.686	20	2.0	2–4	–	0.89
					2–3	0.766	–	–	–	–	–
					2–3	0.733	–	–	–	–	–

Note: *from Palomino et al., 2008, **from correlations and experimental data: Jones and Owens, 1980; Ghanizadeh et al., 2014; Gensterblum et al., 2014.

and analysis of all results in order to identify common trends and behavior. All pressure signatures are provided in Supplementary Material 1.

4.1. Typical response – breakthrough pressure

Fig. 3 shows the response of a kaolinite specimen. The CO₂ pressure is increased in steps (Fig. 3a). There are three main stages: pressurization, breakthrough and flushing. A descriptive analysis follows.

- (a) **Pressurization:** The pressure difference $\Delta P = P_{in} - P_{out}$ is below the breakthrough pressure P_c^* , $\Delta P < P_c^*$. The CO₂-water interface surrounds the specimen, compresses the sediment, the void ratio e decreases $de/dt < 0$, and pushes out water $dm_w/dt > 0$ following each differential pressure increase. The clay plug contracts but does not allow CO₂ invasion so that it performs as a perfect seal (Fig. 3b). Volume contraction and water displacement decay in time towards $dm_w/dt \sim 0$ and $de/dt \sim 0$.
- (b) **Breakthrough:** Pressure reaches the breakthrough pressure $\Delta P > P_c^*$ (refer to Eq. (1)). In this test, breakthrough is detected after ~70 days when there is a sudden increase in CO₂ flow downstream $q_{CO_2} > 0$ (Fig. 3c). The rate of water flow vanishes after CO₂ breakthrough (Fig. 3b). The CO₂ flow rate remains stable for the first ~8 days and then decays due to the decrease in reservoir pressure after breakthrough (Fig. 3c). The measured sediment strain $\varepsilon_z = \Delta z/h$ allow us to compute the void ratio evolution $e = e_o - \varepsilon_z(1 + e_o)$ from the initial void ratio e_o , (Fig. 3d – volume average void ratio).
- (c) **CO₂ flush:** A high differential pressure ΔP forces dry CO₂ advection through the sediment plug $q_{CO_2} > 0$. The average backpressure P_{out} is raised to 6.5 MPa during the flushing stage of this kaolinite specimen (Fig. 3a).

4.2. Parametric study

4.2.1. Breakthrough pressure

Table 3 summarizes all breakthrough pressures measured in this study; the reported pressure interval indicates the initial reservoir pressure at the beginning of the new pressure stage, and the last pressure sustained by the specimen without breakthrough. Fig. 4 shows the experimentally measured breakthrough pressures P^* for all specimens as a function of the average pore throat diameter $\mu(d)$ estimated from either specific surface S_s or mean grain size D_{50}

$$\mu(d) = 2e/(S_s\rho) \text{ fine grained} \quad (2)$$

$$\mu(d) = 0.15D_{50} \text{ coarse grained (cubic tetrahedral packing)} \quad (3)$$

To facilitate the analysis, measured values are scaled by the corresponding pressure-dependent interfacial tension (provided in Supplementary Material 2) to a reference $T_s = 0.025 \text{ N/m}$. Breakthrough values reported in the literature are superimposed on Fig. 4 (also PT-corrected to $T_s = 0.025 \text{ N/m}$); in this case, the mean pore size is estimated from reported permeability and porosity data $\mu(d) \sim 8(k_w/n)^{1/2}$ (Table 3). Fig. 4 also provides theoretical trends computed with Laplace's equation (Eq. (1) – $T_s = 0.025 \text{ N/m}$ and $\cos(\theta) = 1$). The breakthrough pressure measured in montmorillonitic sediments and values reported for tight rocks in the literature are lower than breakthrough pressures estimated using Laplace's equation; this may result from spatially correlated pore-size variability, dual porosity (unaccounted for in mean estimates), and underlying pore-scale processes during percolation that are not taken into consideration in quasi-static analyses.

4.2.2. Permeability

We compute the water permeability k_w from early CO₂ pressurization stages before breakthrough assuming incompressible flow with radial symmetry. The CO₂ sediment permeability after breakthrough k_{CO_2} is estimated using the measured CO₂ mass flow rate q_{CO_2} [kg/s], a Klinkenberg slip-flow correction factor b , and assumes axisymmetric

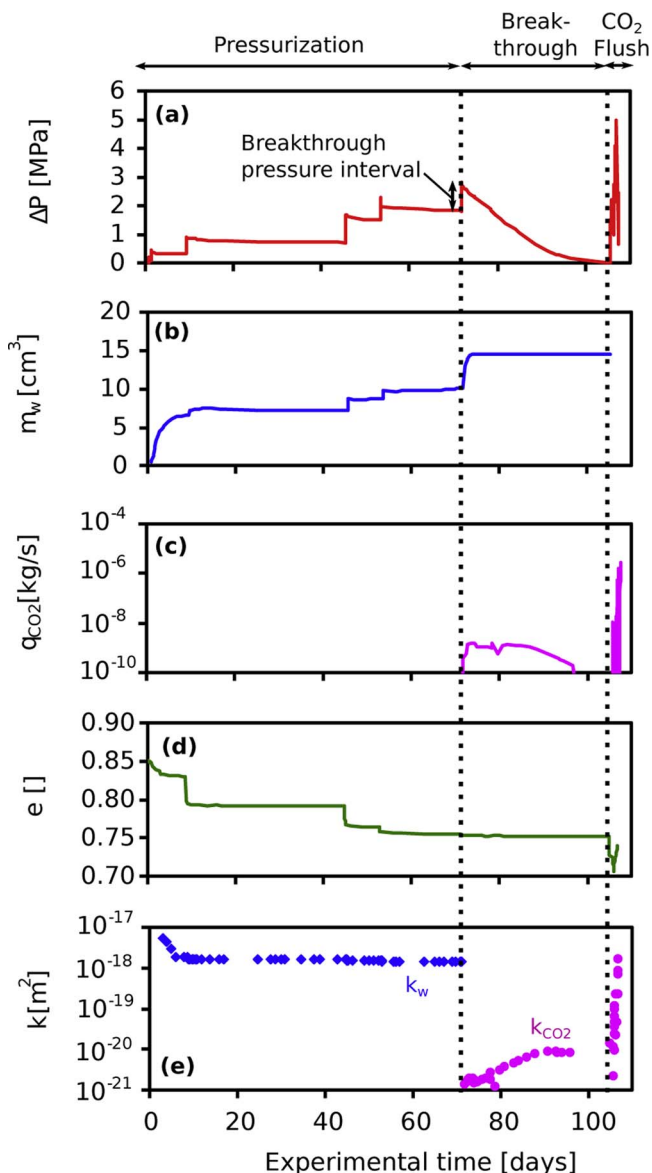


Fig. 3. Typical plug response. (a) Differential pressure $\Delta P = P_{in} - P_{out}$. (b) Displaced water volume m_w . (c) CO_2 flow rate q_{CO_2} . (d) Specimen void ratio $e = f(\Delta z)$. (e) CO_2 permeability k_{CO_2} . As the fluid pressure-difference increases, CO_2 attempts to invade the porous medium; eventually CO_2 penetrates the sediment, displaces water $dm_w/dt > 0$, percolates and flows through the specimen $q_{\text{CO}_2} > 0$. Capillarity promotes volumetric contraction $de/dt < 0$ after breakthrough. Specimen: kaolinite RP2.

ideal gas flow towards the central collecting pipe,

$$k_{\text{CO}_2} = \frac{q_{\text{CO}_2 \text{ out}} \bar{\mu}_{\text{CO}_2} P_{\text{out}} \ln(d_c/d_p)}{2\pi h \rho_{\text{CO}_2 \text{ out}} (P_{\text{in}}^2 - P_{\text{out}}^2) [1 + 2b/(P_{\text{in}} + P_{\text{out}})]} \quad (4)$$

where $\bar{\mu}_{\text{CO}_2}$ [Pa s] is the average CO_2 viscosity (typically 1.4×10^{-5} Pa s to 1.5×10^{-5} Pa s at laboratory temperature and $P < 5$ MPa), $\rho_{\text{CO}_2 \text{ out}}$ [kg/m³] is the CO_2 mass density downstream, h is the specimen height, P_{in} and P_{out} are the upstream and downstream pressures, $d_c \sim 40$ mm is the specimen diameter, and $d_p = 3.17$ mm is the collection pipe diameter. Values of the Kinklenberg correction factor b are listed in Table 3. Fig. 3e shows the estimated CO_2 permeability k_{CO_2} for a kaolinite specimen after breakthrough: permeability increases after breakthrough because the injection of dry CO_2 gradually displaces water and decreases the specimen water saturation.

Table 3 summarizes all permeability values measured in this study. The water permeability k_w in clay plugs varies from $\sim 10^{-20}$ m² to 10^{-18} m². The CO_2 permeability k_{CO_2} of the clay plugs ranged from

10^{-21} m² to 10^{-19} m² after breakthrough (Table 3). The interval shown for CO_2 permeability captures the evolution in permeability from the initial value shortly after breakthrough to the peak value measured after breakthrough. The CO_2 permeability increased up to 7 times during gas- CO_2 flushing after breakthrough, while liquid- CO_2 flushing had a more pronounced effect and increased the CO_2 permeability more than 200 times (Table 3). The CO_2 relative permeability remains lower than ~ 0.2 in the absence of fractures. Yet, even in the presence of localized fluid flow, the CO_2 permeability in tight sediment packs remains small $k_{\text{CO}_2} < 10^{-18}$ m² and may decrease by “healing” under high effective stress (Fig. 3e).

Fig. 5 shows water/absolute permeabilities and CO_2 permeabilities after breakthrough for all specimens tested in this study, and values collected from the literature. In general, the overall trend is an increase in permeability as the mean pore size increases. Theoretical and empirical models scale permeability with the square of the pore size (Hazen 1892; Kozeny 1927); lines drawn with 2:1 slope on Fig. 5 capture this observation (see effect of specific surface in (Ren et al., 2016) and (Ren and Santamarina 2017)).

Capillary-driven contraction and low final water saturation $S_w \sim 0.5$ after liquid CO_2 invasion and flushing indicate sediment desiccation (e.g., the kaolinite RP2 specimen experienced $\Delta e = -0.02$). On the other hand, high CO_2 relative permeabilities $k_{\text{CO}_2}/k_w \geq 1$ together with high residual water saturation after CO_2 breakthrough-&-flushing suggest the development of fractures; this was the case with one bentonite specimen that exhibited a fracture during the forensic analysis after test completion (Note: all other specimens showed mechanical integrity).

4.3. Discussion of experimental results and application to geological systems

Our experimental results highlight the relationship between breakthrough pressure and permeability with grain size and expected average pore size in relatively homogeneous and uniformly sized sediment packs. Geological formations are usually heterogeneous, laminated, and may exhibit structural discontinuities such as faults, fractures, and fluid escape pipes. Hence, measurements reported here yield upper-bound estimates of seal capacity.

Given the imposed boundary conditions, pressure and water saturation change during a given test, and permeability is not linear with the inverse of the average pressure. Therefore, the Klinkenberg correction factor b for slip-flow in Eq. (4) is estimated using correlations; adopted factors compare well with typical values reported in the literature for similar porous media.

Previous breakthrough experiments (Table 2) conducted with supercritical CO_2 agree with our experimental results after normalization for interfacial tension. Thus, the assumption of similar contact angle holds for the mineral systems compared in this study. Significant variations of wettability with pressure may occur in oil-wet or organic-rich mineral systems (Espinoza and Santamarina, 2011; Arif et al., 2017; Guiltinan et al., 2017). Changes in wettability from water-wet to CO_2 -wet may facilitate breakthrough.

Both the “incremental pressure increase” method (this study; Horseman et al., 1999; Li et al., 2005) and the “residual pressure difference” method (Hildenbrand et al., 2002, 2004; Makhnenko et al., 2017) yield results in the same order of magnitude. The residual pressure method may underestimate the breakthrough pressure by $\sim 50\%$ (Boulin et al., 2013). Experiments should recreate the initial effective stress conditions in-situ. High pressure gradients often adopted for short-time laboratory studies cause an opposite effective stress gradient; the ensuing low effective stress at the inlet enhances the effects of open cracks and promotes hydraulic fracturing of the sediment plug. In this study, we measure breakthrough pressure and permeability parallel to bedding. Particle alignment in clay mudrocks leads to higher transport properties parallel to bedding than normal to bedding.

Typically, the sealing-capacity of hydrocarbon-bearing geological

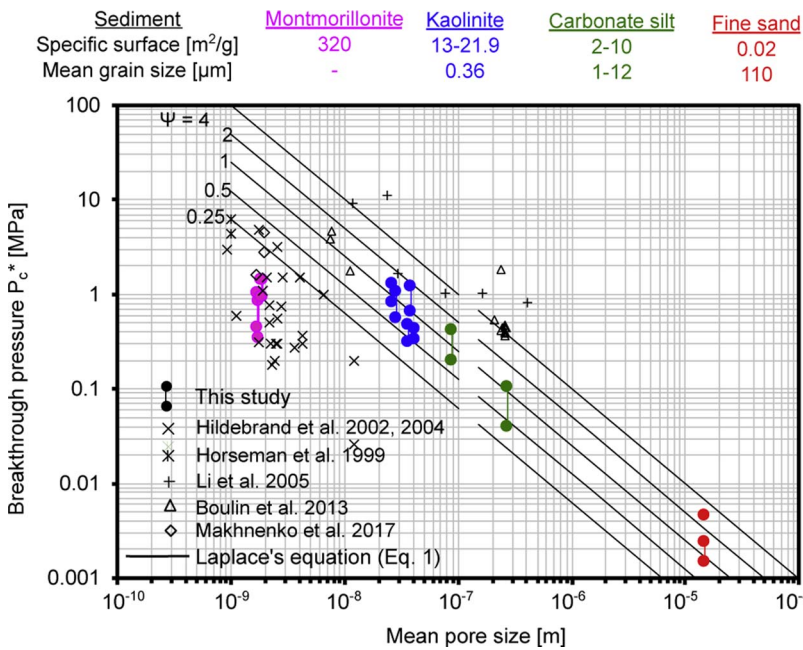


Fig. 4. Experimental breakthrough pressure as a function of the mean pore size (this study and values extracted from published data). Predicted breakthrough pressures are superimposed for different values of the geometric fabric factor ψ (Lines – Eq. (1)). All breakthrough pressures are scaled for $T_s = 0.025 \text{ N/m}$. The montmorillonite specimens exhibit significantly lower breakthrough pressures than anticipated.

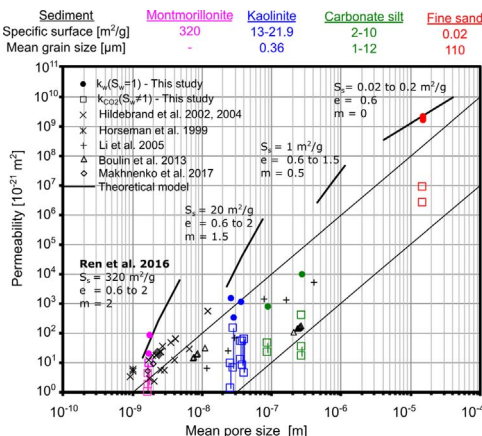


Fig. 5. Water and CO_2 permeability after breakthrough for tested sediment packs as a function of the characteristic pore size. The lines at 2:1 slope correspond to theoretical models. Additional line segments capture the role of specific surface (m is porosity exponent – (Ren et al., 2016)).

formations is assessed through the entry pressure in mercury intrusion porosimetry (Schowalter 1979; Schlömer and Kross, 1997). This approach underestimates the actual breakthrough pressure in systems with a non-uniform pore size distribution (Schlömer and Kross, 1997; Li et al., 2005). Furthermore, mercury intrusion cannot discriminate bedding-induced anisotropy and invades granules parallel to bedding. Finally, the interpretation of capillary pressures estimated using mercury intrusion must take into consideration differences in contact angles for CO_2 or hydrocarbon systems: natural oil and gas-bearing formations are typically less sealing to CO_2 than to CH_4 and oil because of lower interfacial tension for CO_2 -brine than for methane-brine and for oil-brine.

5. Implications – caprock integrity and CO_2 leaks

This section explores the sealing capacity of caprocks, and anticipates expected leak and storativity ratings for various caprocks at current and target CO_2 storage sites based on the reported mineralogical, petrophysical, and geometrical properties of the caprocks, reservoirs and expected CO_2 plumes (see Table 1). We complement

available data with data from our experimental work. Values are upper-bound estimates of the sealing properties since the analysis does not take into account caprock heterogeneity and structural discontinuities.

5.1. Leak estimation

Buoyancy and CO_2 diffusive transport remain in the long term, long after the injection excess pressure vanishes. Consider a formation overlaid by a continuous caprock of thickness t_h [m]. The time to achieve steady state diffusive flux is inversely proportional to the CO_2 diffusion coefficient D^* [m^2/s], $T_{\text{diff}} = t_h^2/D^* \sim 32$ years for a 1 m caprock and ~ 3200 years for a 10 m caprock, assuming $D^* = 10^{-9} \text{ m}^2/\text{s}$ (similar to CH_4 values obtained by Schlömer and Krooss, 1997). Thereafter and in the absence of chemical reactions, the steady-state diffusive flux $q_{\text{CO}_2}^{\text{diff}}$ [$\text{kg}/\text{m}^2/\text{s}$] is calculated using Fick's law,

$$q_{\text{CO}_2}^{\text{diff}} = -nD^* \frac{\Delta x_{\text{CO}_2}}{t_h} \quad (5)$$

where Δx_{CO_2} is the difference in CO_2 concentration in water above and below the caprock $\Delta x_{\text{CO}_2} < \sim 0.044 \text{ kg}(\text{CO}_2)/\text{m}^3(\text{water})$, and $n [-]$ is the caprock porosity (assumed $n = 0.1$; the tortuosity coefficient is neglected in this approximation). Fig. 6a shows the diffusive flux for various caprock thicknesses (1 m, 10 m and 100 m). These baseline estimates are significantly lower than the “reference leak rate” of $3 \text{ kg}/\text{m}^2/\text{yr}$ needed to saturate a 100 m sediment column with CO_2 in 100 years (discussed in the Introduction).

On the other hand, the advective mass flow rate of CO_2 after breakthrough $q_{\text{CO}_2}^{\text{adv}}$ [$\text{kg}/\text{m}^2/\text{s}$] through a caprock thickness t_h [m] can be estimated using Darcy's equation given a pressure gradient ΔP [Pa], so that,

$$q_{\text{CO}_2}^{\text{adv}} = \frac{k k_r^r \rho_{\text{CO}_2} (\Delta P - \rho_{\text{CO}_2} g t_h)}{\mu_{\text{CO}_2} t_h} \quad (6)$$

where k [m^2] is the absolute permeability, k_{CO_2} [–] is the CO_2 relative permeability, ρ_{CO_2} [kg/m^3] is the CO_2 mass density, and μ_{CO_2} [Pa s] is the CO_2 viscosity. Fig. 6a shows predicted fluxes for caprocks with permeability $k \sim 10^{-19} \text{ m}^2$ (equal or higher than values in Tables 1 and 2, and Fig. 5) as a function of total head difference ($\Delta P - \rho_{\text{CO}_2} g t_h$). The resulting advective flow rate is as high as $20 \text{ kg}/\text{m}^2/\text{yr}$ for a thin caprock ($t_h = 1 \text{ m}$). For more realistic field conditions, advective flow rates remain smaller than the “reference leak rate” of $3 \text{ kg}/\text{m}^2/\text{yr}$.

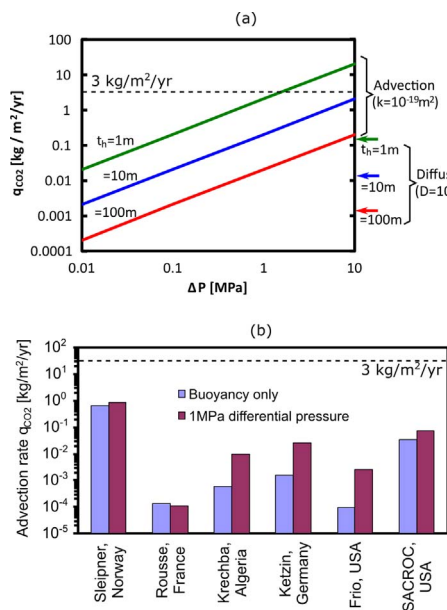


Fig. 6. CO₂ transport through the caprock. (a) Order of magnitude analysis for diffusive transport before breakthrough and advective transport after breakthrough – no fracturing (Eqs. (5) and (6); $n = 0.1$, $D^* = 10^{-9} \text{ m}^2/\text{s}$, $S_{CO_2} = 0.3$, $k_{CO_2} = (S_{CO_2})^2$, $\mu_{CO_2} = 10^{-4} \text{ Pa s}$). Notice that the time to achieve steady state diffusive flux is proportional to t_h^2/D^* . (b) Upper bound advective flow rate estimates for different CO₂ storage sites assuming buoyancy driven flow and a 1 MPa pressure difference. The Kozeny-Carman equation is used to estimate the permeability when direct measurements are not available (Table 1 and Kozeny, 1927). The “reference leak rate” of 3 kg/m²/yr would saturate the pore water in a shallow 100 m sediment column in 100 years (typical porosity of 0.4 – disregards the buffering effects of minerals).

Let us compute the advective flow rate after CO₂ breakthrough for several existent and planned CO₂ storage sites using caprock permeabilities based on reported values and rock descriptions (Table 1). We assume a CO₂ plume height equal to the reservoir thickness and a mass density difference $\rho_w - \rho_{CO_2} = 300 \text{ kg/m}^3$. Fig. 6b shows the calculated advection rates. A post-breakthrough leak rate lower than 0.1 kg/m²/yr is estimated for all cases in the absence of fractures or other flow localization features.

5.2. Storativity rating – dimensionless numbers

The sealing capacity of carbon geological storage systems can be compared in terms of caprock characteristics, plume geometry, and in-situ pore pressure and stresses.

5.2.1. Sealing capacity

The capillary breakthrough pressure P_c^* is an intrinsic caprock property (Eqs. (1) and (2)). On the other hand, the buoyant CO₂ pressure ΔP is determined by the thickness of the continuous CO₂ plume h , $\Delta P = (\rho_w - \rho_{CO_2})gh$. We define the “sealing number” as the capillary breakthrough pressure P_c^* (calculated by combining Eqs. (1) and (2)) divided by the buoyant pressure ΔP ,

$$\text{Sealing number} = \pi_1 = \frac{P_c^*}{\Delta P} = \frac{\psi T_s \cos \theta S_s \rho_m}{2e hg (\rho_w - \rho_{CO_2})}, \quad (7)$$

Sealing numbers $\pi_1 \gg 1$ are sought for safe storage. Fig. 7 shows π_1 -values for selected carbon storage sites. Upper and lower bounds reflect the uncertainty in P_c^* and ΔP . The maximum capillary breakthrough pressure is assumed to be 11.2 MPa in view of experimentally measured breakthrough pressures reported in Table 2. The minimum capillary breakthrough pressure is estimated assuming $\psi = 0.25$ (Fig. 4). The CO₂ plume height can be higher than the reservoir thickness; conversely, the plume height can be a fraction of the reservoir thickness in

thick reservoirs. Hence, bounds plotted in Fig. 7 consider the CO₂ plume height is 3 h for thin reservoirs $h < 50 \text{ m}$ and 0.1 h for thick reservoirs $h > 50 \text{ m}$. The initial excess injection pressure changes this pressure balance during the early life of the storage system. The relatively low sealing number suggested for Sleipner reflects the high void ratio and potentially high plume height. The high capillary sealing number suggested for Frio results from relatively high breakthrough pressure and small reservoir thickness.

5.2.2. Mechanical stability

Variations in pore pressure cause changes in effective stress, can trigger fault reactivation, and fluid-driven open-mode fractures. The stability number compares the initial vertical effective stress σ'_{zo} at the reservoir depth z to the buoyant pressure ΔP created by a CO₂ plume of thickness h (refer to sketch in Fig. 7):

$$\text{Stability number} = \pi_2 = \frac{\sigma'_{zo}}{\Delta P} = \frac{(z_w g \rho_w + z g \rho_{bulk}) - P_o}{hg(\rho_w - \rho_{CO_2})} \quad (8)$$

where z_w is the height of the water column above the seafloor, ρ_{bulk} is the bulk mass density of the sediment column of height z , and P_o is the initial fluid pressure at the reservoir-seal interface. The numerator captures the level of skeletal forces that oppose fluid-driven instabilities. Rigorously, the analysis should be in terms of the least principal effective stress, however, this value is often unknown a priori (Note: the mean stress is ~ 0.5 of the vertical effective stress in the absence of tectonism). A low initial fluid pressure P_o relative to the overburden, such as in depleted reservoirs, favors stable injection; conversely, high P_o values relative to overburden facilitate hydraulic fracturing. The denominator may also include transient pressure increases during injection and pressure build up in compartmentalized reservoirs. Reservoirs with high stability numbers π_2 allow for safe injection and tall CO₂ plumes.

Fig. 7 shows the stability number π_2 estimated for field cases listed in Table 1, taking into consideration the uncertainty in the CO₂ plume height (see π_1 -analysis). The low stability number suggested for Sleipner reflects the low effective stress at shallow depth and the relatively tall potential plume height. On the other hand, the high stability numbers estimated for Frio and Krechba results from the high overburden and relatively small potential for developing tall CO₂ plumes. Injection rates, reservoir compartmentalization, horizontal in-situ stress anisotropy in tectonic regimes, the presence of faults and fractures, complex geological structures, mineral reactivity and depletion history will also affect the stability of the formation.

6. Conclusions

Shales and/or evaporites cap most target CO₂ storage sites. Small pores in high specific surface clay-rich caprocks give rise to high capillary entry pressures and high viscous drag that hinder the migration of buoyant carbon dioxide CO₂.

We measured the breakthrough pressure and ensuing CO₂ permeability through sediment plugs, and monitored their volumetric deformation using high-pressure oedometer cells. The data show water expulsion and volumetric contraction prior to CO₂ breakthrough, followed by preferential CO₂ flow thereafter.

Our experimental results and data gathered from previous studies highlight the inverse relationship between breakthrough pressure and pore size. The Laplace equation over predicts the capillary breakthrough pressure when the mean pore size is used. Apparently, CO₂ invades along percolating paths made of the larger pores; thus, a higher percentile should be used to estimate the breakthrough pressure instead of the mean pore size.

In terms of macro-scale parameters, the breakthrough pressure increases as the sediment specific surface increases and the porosity decreases. The maximum breakthrough pressure is $\sim 6.2 \text{ MPa}$ in

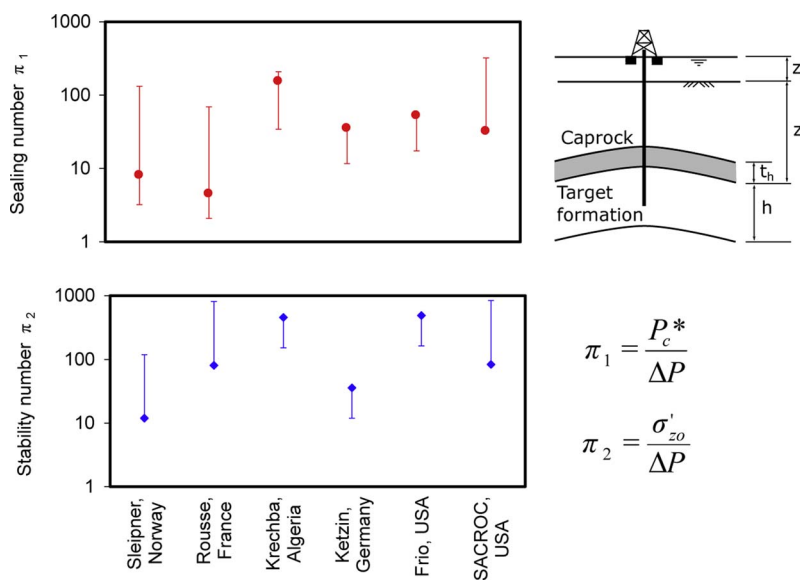


Fig. 7. Analysis of the caprock sealing capacity at current and planned CO₂ storage sites. Results are plotted in terms of the sealing number π_1 between the capillary pressure and the buoyant pressure (Eq. (7)), and the stability number π_2 between the effective vertical stress and the buoyant pressure (Eq. (8)). The circle corresponds to a plume height equal to the reservoir thickness. The error bars represent uncertainty in capillary pressure and buoyancy (refer to text). P_c^* is available from experimental data in Table 1 (Rousse, Frio, Ketzin) or calculated with Eq. (7) otherwise. Effective overburden stress, caprock thickness, and CO₂ storage capacity are key parameters for evaluating the safety of storage sites.

argillaceous formations, and up to 11.2 MPa in evaporites. Fluid-driven open-mode fractures limit the capillary breakthrough pressure in montmorillonite plug experiments.

The CO₂ permeability after breakthrough is significantly lower than the absolute permeability, but it may increase in time due to desiccation. Most specimens showed a water saturation of 0.7–0.9 after breakthrough, and a CO₂ relative permeability smaller than 0.2.

Leakage will be advection-controlled once percolation takes place at most storage sites being considered. Diffusive and advective CO₂ leaks through non-fractured caprocks will be minor and will not compromise the storage capacity at CO₂ injection sites.

The viability of potential storage sites depends on: the initial fluid pressure, the buoyant pressure caused by the CO₂ plume, the capillary breakthrough pressure of the caprock, and the stress conditions at the reservoir depth. These parameters combine into the “sealing number” and the “stability number”. These two dimensionless numbers provide a rapid assessment of the geological formation under consideration.

This analysis focused on chemically stable, homogeneous and continuous seal layers. However, CO₂ acidifies water and triggers mineral dissolution that can modify pore structure and cause variations in breakthrough percolating paths and permeability (Kim and Santamarina, 2014). Furthermore, recent studies highlight the role of spatial variability when evaluating the CO₂ plume evolution and potential CO₂ leaks (Couësan et al., 2013; Cavanagh and Haszeldine, 2014; Cartwright and Santamarina, 2015). Unexpected CO₂ migration patterns detected in the Decatur and Sleipner field projects prompt us to select sites with redundant seal layers for the safe and long-term storage of CO₂.

Acknowledgements

This research was performed at the Georgia Institute of Technology with support from the U.S. Department of Energy (DOE) under grant number DE-FE0001826. Complimentary work at The University of Texas at Austin was supported as part of the Center for Frontiers of Subsurface Energy Security (CFSES) funded by the U. S. Department of Energy under Award # DE-SC0001114. Additional support was provided by the The Goizueta Foundation and the KAUST Endowment. Any opinions, findings, conclusions, or recommendations expressed herein are those of the authors and do not necessarily reflect the views of funding organizations.

Appendix A. Supplementary data

Supplementary data associated with this article can be found, in the online version, at <http://dx.doi.org/10.1016/j.ijggc.2017.09.019>.

References

- Allis, R.G., Chidsey, T., Gwynn, W., Morgan, C., White, S.P., Adams, M., Moore, J., 2001. Natural CO₂ reservoirs on the Colorado Plateau and Southern Rocky Mountains: candidates for CO₂ sequestration. In: Paper Presented at 1st National Conf. on Carbon Sequestration. May 14–17, 2001, DOE-NETL, Washington DC.
- Alonso, E.E., Gens, A., Josa, A., 1990. A constitutive model for partially saturated soils. *Geotechnique* 40 (3), 405–430.
- Angeli, M., Soldal, M., Skurtveit, E., Aker, E., 2009. Experimental percolation of supercritical CO₂ through a caprock. *Energy Procedia* 1 (1), 3351–3358.
- Arif, M., Lebedev, M., Barifciani, A., Iglauser, S., 2017. Influence of shale-total organic content on CO₂ geo-storage potential. *Geophys. Res. Lett.* s1. <http://dx.doi.org/10.1002/2017GL073532>.
- Armitage, P.J., Worden, R.H., Faulkner, D.R., Aplin, A.C., Butcher, A.R., Iliffe, J., 2010. Diagenetic and sedimentary controls on porosity in Lower Carboniferous fine-grained lithologies, Krichba field, Algeria: a petrological study of a caprock to a carbon capture site. *Mar. Petrol. Geol.* 27 (7), 1395–1410.
- Bøe, R., Zweigel, P., 2001. Characterisation of the Nordland Shale in the Sleipner area by XRD analysis – A contribution to the Saline Aquifer CO₂ Storage (SACS) project. SINTEF Rep. 33, 0764.
- Bachu, S., Bennion, B.I., 2008. Effects of in-situ conditions on relative permeability characteristics of CO₂-brine systems. *Environ. Geol.* 54 (8), 1707–1722.
- Benson, S.M., Cole, D.R., 2008. CO₂ sequestration in deep sedimentary formations. *Elements* 4 (5), 325–331.
- Bergmo, P.E.S., Grimstad, A.-A., Lindeberg, E., 2011. Simultaneous CO₂ injection and water production to optimise aquifer storage capacity. *Int. J. Greenhouse Gas Control* 5 (3), 555–564.
- Berne, P., Bachaud, P., Fleury, M., 2010. Diffusion properties of carbonated caprocks from the Paris basin. *Oil Gas Sci. Technol.-Revue De L Institut Francais Du Petrole* 65 (3), 473–484.
- Boulin, P.F., Bretonnier, P., Vassil, V., Samouillet, A., Fleury, M., Lombard, J.M., 2013. Sealing efficiency of caprocks: experimental investigation of entry pressure measurement methods. *Mar. Petrol. Geol.* 48, 20–30.
- Burland, J.B., 1990. On the compressibility and shear strength of natural clays. *Geotechnique* 40, 329–378.
- Busch, A., Bertier, P., Gensterblum, Y., Rother, G., Spiers, C.J., Zhang, M., Wentink, H.M., 2016. On sorption and swelling of CO₂ in clays. *Geomech. Geophys. Geo-Energy Geo-Resour.* 2 (2), 111–130.
- Carey, J.W., Wigand, M., Chipera, S.J., WoldeGabriel, G., Pawar, R., Lichtner, P.C., Wehner, S.C., Raines, M.A., Guthrie, J.G.D., 2007. Analysis and performance of oil well cement with 30 years of CO₂ exposure from the SACROC Unit, West Texas, USA. *Int. J. Greenhouse Gas Control* 1 (1), 75–85.
- Cartwright, J., Santamarina, C., 2015. Seismic characteristics of fluid escape pipes in sedimentary basins: implications for pipe genesis. *Mar. Petrol. Geol.* 65, 126–140.
- Cavanagh, A.J., Haszeldine, R.S., 2014. The Sleipner storage site: capillary flow modeling of a layered CO₂ plume requires fractured shale barriers within the Utsira Formation. *Int. J. Greenhouse Gas Control* 21, 101–112.
- Chadwick, R.A., Zweigel, P., Gregersen, U., Kirby, G.A., Holloway, S., Johannessen, P.N., 2004. Geological reservoir characterization of a CO₂ storage site: The Utsira Sand, Sleipner, Northern North Sea. *Energy* 29 (9–10), 1371–1381.

- Chalbaud, C., Robin, M., Lombard, J.M., Martin, F., Egermann, P., Bertin, H., 2009. Interfacial tension measurements and wettability evaluation for geological CO₂ storage. *Adv. Water Resour.* 32 (1), 98–109.
- Chang, Y.B., Lim, M.T., Pope, G.A., Sepehrnoori, K.I., 1994. CO₂ flow patterns under multiphase flow: heterogeneous field-scale conditions. *SPE Reservoir Eng.* 9 (03), 208–216.
- Chi, S.M., Morsi, B.I., Klinzing, G.E., Chiang, S.H., 1988. Study of interfacial properties in the liquid CO₂ water coal system. *Energy Fuels* 2 (2), 141–145.
- Chiaramonte, L., Zoback, M., Friedmann, J., Stamp, V., 2008. Seal integrity and feasibility of CO₂ sequestration in the Teapot Dome EOR pilot: geomechanical site characterization. *Environ. Geol.* 54 (8), 1667–1675.
- Chiodini, G., Frondini, F., Marini, L., 1995. Theoretical geothermometers and CO₂ indicators for aqueous solutions coming from hydrothermal systems of medium-low temperature hosted in carbonate-evaporite rocks. Application to the thermal springs of the Etruscan Swell, Italy. *Applied Geochemistry* 10 (3), 337–346.
- Chiquet, P., Broseta, D., Thibault, S., 2007. Wettability alteration of caprock minerals by carbon dioxide. *Geofluids* 7 (2), 112–122.
- Choens, R.C., Dewers, T., Ilgen, A.G., Espinoza, D.N., 2016. The Effect of Hydrous Supercritical Carbon Dioxide on the Mohr Coulomb Failure Envelope in Boise sandstone. AGU Fall Meeting.
- Chong, S.H., Santamarina, J.C., 2016. Soil compressibility models for a wide stress range. *J. Geotech. Geoenviron. Eng.* 142 (6), 06016003.
- Consoli, C.P., Wildgust, N., Causebrook, R., 2015. Global Storage Readiness Assessment – An Approach to Assessing National Readiness for Wide-scale Deployment of CO₂ Geological Storage Projects. Global Carbon Capture and Storage Inst. Ltd.
- Couëslan, M.L., Ali, S., Campbell, A., Nutt, W.L., Leaney, W.S., Finley, R.J., Greenberg, S.E., 2013. Monitoring CO₂ injection for carbon capture and storage using time-lapse 3D VSPs. *Lead. Edge* 32 (10), 1268–1276.
- De Paola, N., Faulkner, D.R., Collettini, C., 2009. Brittle versus ductile deformation as the main control on the transport properties of low-porosity anhydrite rocks. *J. Geophys. Res.: Solid Earth* 114 (B6).
- Dewhurst, D.N., Jones, R.M., Raven, M.D., 2002. Microstructural and petrophysical characterization of Muderong Shale: application to top seal risking. *Pet. Geosci.* 8 (4), 371–383. <http://dx.doi.org/10.1144/petgeo.1148.1144.1371>.
- Downey, M.W., 1984. Evaluating seals for hydrocarbon accumulations. *AAPG Bull.* 68 (11), 1752–1763.
- Ehlil-Economides, C., Economides, M.J., 2010. Sequestering carbon dioxide in a closed underground volume. *J. Petrol. Sci. Eng.* 70 (1–2), 118–125.
- Emberley, S., Hutcheon, M., Shevalier, K., Gunter, W.D., Perkins, E.H., 2004. Geochemical monitoring of fluid-rock interaction and CO₂ storage at the Weyburn CO₂-injection enhanced oil recovery site, Saskatchewan, Canada. *Energy* 29 (9–10), 1393–1401.
- Espinoza, D.N., Santamarina, J.C., 2010. Water-C-mineral systems: interfacial tension, contact angle and diffusion–Implications to CO₂ geological storage. *Water Resour. Res.* 46 (W07537). <http://dx.doi.org/10.1029/2009WR008634>.
- Espinoza, D.N., Santamarina, J.C., 2012. Clay interaction with liquid and supercritical CO₂: the relevance of electrical and capillary forces. *Int. J. Greenh. Gas Control* 10, 351–362.
- Förster, A., Springer, N., Beutler, G., Luckert, J., Norden, B., Lindgren, H., 2007. The mudstone-dominated caprock system of the CO₂-storage site at Ketzin, Germany, paper presented at AAPG Annual Convention, Long Beach, California.
- Fenghour, A., Wakeham, W.A., Vesovic, V., 1998. The viscosity of carbon dioxide. *J. Phys. Chem. Ref. Data* 27 (1), 31–44.
- Fleury, M., et al., 2010. Evaluating sealing efficiency of caprocks for CO₂ storage: an overview of the geocarbone-integrity program and results. *Oil Gas Sci. Technol. Revue De L'Institut Français Du Pétrole* 65 (3), 435–444.
- Gaus, I., Azaroual, M., Czernichowski-Lauriol, I., 2005. Reactive transport modelling of the impact of CO₂ injection on the clayey caprock at Sleipner (North Sea). *Chem. Geol.* 217 (3–4), 319–337.
- Gensterblum, Y., Ghazizadeh, A., Krooss, B.M., 2014. Gas permeability measurements on Australian subbituminous coals: fluid dynamic and poroelastic aspects. *J. Nat. Gas Sci. Eng.* 19, 202–214.
- Ghanizadeh, A., Gasparik, M., Amann-Hildenbrand, A., Gensterblum, Y., Krooss, B.M., 2014. Experimental study of fluid transport processes in the matrix system of the European organic-rich shales: I. Scandinavian Alum Shale. *Mar. Petrol. Geol.* 51, 79–99.
- Gherardi, F., Xu, T.F., Pruess, K., 2007. Numerical modeling of self-limiting and self-enhancing caprock alteration induced by CO₂ storage in a depleted gas reservoir. *Chem. Geol.* 244 (1–2), 103–129.
- Gueguen, Y., Palciauskas, V., 1994. Introduction to the Physics of Rocks. Princeton University Press.
- Guitinan, E., Cardenas, M.B., Bennett, P.C., Zhang, T., Espinoza, D.N., 2017. The effect of organic matter and thermal maturity on the wettability of supercritical CO₂ on organic shales. *Int. J. Greenh. Gas Control* 65, 15–22.
- Gunter, W.D., Perkins, E.H., Hutcheon, I., 2000. Aquifer disposal of acid gases: modelling of water-rock reactions for trapping of acid wastes. *Appl. Geochem.* 15 (8), 1085–1095.
- Han, W.S., McPherson, B.J., Lichtner, P.C., Wang, F.P., 2010. Evaluation of trapping mechanisms in geologic CO₂ sequestration: case study of SACROC northern platform, a 35-year CO₂ injection site. *Am. J. Sci.* 310 (4), 282–324.
- Hazen, A., 1892. Some Physical Properties of Sands and Gravels, with Special Reference to Their Use in Filtration. pp. 539–556 24th Annual Rep., Massachusetts State Board of Health, Pub. Doc. No. 34.
- Heller, R., Zoback, M., 2014. Adsorption of methane and carbon dioxide on gas shale and pure mineral samples. *J. Unconventional Oil Gas Resour.* 8, 14–24.
- Hildenbrand, A., Scholmer, S., Krooss, B.M., 2002. Gas breakthrough experiments on fine-grained sedimentary rocks. *Geofluids* 2 (1), 3–23.
- Hildenbrand, A., Scholmer, S., Krooss, B.M., Littke, R., 2004. Gas breakthrough experiments on pelitic rocks: comparative study with N-2, CO₂ and CH₄. *Geofluids* 4 (1), 61–80.
- Horseman, S.T., Harrington, J.F., Sellin, P., 1999. Gas migration in clay barriers. *Eng. Geol.* 54 (1–2), 139–149.
- Hovorka, S.D., 2009. Frio brine pilot: the first U.S. sequestration test, Southwest Hydrology, September/October.
- IPCC, 2005. In: Metz, B., Davidson, O., de Coninck, H.C., Loos, M., Meyer, L.A. (Eds.), *IPCC Special Report on Carbon Dioxide Capture and Storage*. Prepared by Working Group III of the Intergovernmental Panel on Climate Change. Cambridge University Press Cambridge, United Kingdom and New York, NY, USA 442 pp.
- Iglauer, S., Pentland, C.H., Busch, A., 2015. CO₂ wettability of seal and reservoir rocks and the implications for carbon geo-sequestration. *Water Resour. Res.* 51 (1), 729–774.
- Jones, F.O., Owens, W.W., 1980. A laboratory study of low-permeability gas sands. *J. Pet. Technol.* 32 (9), 1631–1640 SPE-7551-PA.
- Jung, H., Singh, G., Espinoza, D.N., Wheeler, M., 2017. An integrated case study of the Frio CO₂ sequestration pilot test for safe and effective carbon storage including compositional flow and geomechanics. *SPE-182710-MS. SPE Reservoir Simulation Conference*.
- Kampman, N., Busch, A., Bertier, P., Snipe, J., Hangx, S., Pipich, V., Di, Z., Rother, G., Harrington, J.F., Evans, J.P., Maskell, A., Chapman, H.J., Bickle, M.J., 2016. Observational evidence confirms modelling of the long-term integrity of CO₂-reservoir caprocks. *Nat. Commun.* 7, 12268. <http://dx.doi.org/10.1038/ncomms12268>.
- Kaszuba, J.P., Janecky, D.R., Snow, M.G., 2005. Experimental evaluation of mixed fluid reactions between supercritical carbon dioxide and NaCl brine: relevance to the integrity of a geologic carbon repository. *Chem. Geol.* 217 (3–4), 277–293.
- Katsube, T.J., Williamson, M.A., 1994. Effects of diagenesis on shale nano-pore structure and implications for sealing capacity. *Clay Miner.* 29 (4), 451–461.
- Kiessling, D., Schmidt-Hattenberger, C., Schuett, H., Schilling, F., Krueger, K., Schoebel, B., Danckwardt, E., Kummerow, J., CO2SINK Group, 2010. Geoelectrical methods for monitoring geological CO₂ storage: first results from cross-hole and surface-down-hole measurements from the CO₂ SINK test site at Ketzin (Germany). *Int. J. Greenh. Gas Control* 4 (5), 816–826.
- Kim, S., Santamarina, J.C., 2014. CO₂ geological storage: hydro-chemo-mechanical analyses and implications. *Greenhouse Gases: Sci. Technol.* 4 (4), 528–543.
- Kneafsey, T.J., Pruess, K., 2010. Laboratory flow experiments for visualizing carbon dioxide-induced, density-driven brine convection. *Transp. Porous Media* 82 (1), 123–139.
- Kozeny, J.I., 1927. Ueber kapillareleitung des wassers im boden. *Wien Akad. Wiss.* 136 (2a), 271.
- Kvamme, B., Kuznetsova, T., Hebach, A., Oberhof, A., Lunde, E., 2007. Measurements and modelling of interfacial tension for water plus carbon dioxide systems at elevated pressures. *Comput. Mater. Sci.* 38 (3), 506–513.
- Li, S., Dong, M., Li, Z., Huang, S., Qing, H., Nickel, E., 2005. Gas breakthrough pressure for hydrocarbon reservoir seal rocks: implications for the security of long-term CO₂ storage in the Weyburn field. *Geofluids* 5 (4), 326–334.
- Lloret, A., Villar, M.V., Sanchez, M., Gens, A., Pintado, X., Alonso, E.E., 2003. Mechanical behaviour of heavily compacted bentonite under high suction changes. *Geotechnique* 53 (1), 27–40.
- Lyklema, J., 1995. Fundamentals of Interface and Colloid Science. Volume II: Solid-liquid Interfaces. Academic Press New York.
- Lynch, F.L., 1997. Frio shale mineralogy and the stoichiometry of the smectite-to-illite reaction: the most important reaction in clastic sedimentary diagenesis. *Clays Clay Miner.* 45 (5), 618–631.
- Makhnenko, R.Y., Vilarrasa, V., Mylnikov, D., Laloui, L., 2017. Hydromechanical aspects of CO₂ breakthrough into clay-rich caprock, Energia Procedia. In: Proceedings of the 13th International Conference on Greenhouse Gas Control Technologies, GHGT-13. 14–18 November 2016, Lausanne, Switzerland.
- Mathieson, A., Midgley, J., Dodds, K., Wright, I., Ringrose, P., Saoul, N., 2010. CO₂ sequestration monitoring and verification technologies applied at Kerechba, Algeria. *Lead. Edge* 29 (2), 216–222.
- McGrail, B.P., Schaef, H.T., Glezakou, V.A., Dang, L.X., Owen, A.T., 2009. Water reactivity in the liquid and supercritical CO₂ phase: has half the story been neglected? *Energy Procedia* 1 (1), 3415–3419.
- Meckel, T.A., Bryant, S.L., Ganesh, P.R., 2015. Characterization and prediction of CO₂ saturation resulting from modeling buoyant fluid migration in 2D heterogeneous geologic fabrics. *Int. J. Greenhouse Gas Control* 34, 85–96.
- Nygard, R., Gutierrez, M., Hoeg, K., Bjorlykke, K., 2004. Influence of burial history on microstructure and compaction behaviour of Kimmeridge clay. *Pet. Geosci.* 10 (3), 259–270.
- Palaca, S., Socolow, R., 2004. Stabilization wedges: solving the climate problem for the next 50 years with current technologies. *Science* 305 (5686), 968–972.
- Palomino, A.M., Burns, S.E., Santamarina, J.C., 2008. Mixtures of fine-grained minerals?kaolinite and carbonate grains. *Clays and Clay Minerals* 56 (6), 599–611.
- Pentland, C.H., El-Maghrary, R., Georgiadis, A., Iglauer, S., Blunt, M.J., 2011. Immiscible displacements and capillary trapping in CO₂ storage. *Energy Procedia* 4, 4969–4976.
- Peters, E.J., 2012. Advanced Petrophysics: Volume 1: Geology, Porosity, Absolute Permeability, Heterogeneity and Geostatistics. Live Oak Book Co, Austin, Texas.
- Phadnis, H.S., Santamarina, J.C., 2011. Bacteria in sediments: pore size effects. *Geotechn. Lett.* 1 (4), 91–93.
- Pillitteri, A., Cerasi, P., Stavrum, J., Zweigert, P., Bøe, R., 2003. Rock mechanical tests of shale samples from the caprock of the Utsira Sand in well 15/9-A11Rep. SINTEF Petrol. Res.

- Ren, X.-W., Santamarina, J.C., 2017. Hydraulic conductivity in sediments. *J. Eng. Geol.* (In print).
- Ren, Q.Y., Chen, G.J., Yan, W., Guo, T.M., 2000. Interfacial Tension of (CO₂ + CH₄) plus water from 298 K to 373 K and pressures up to 30 MPa. *J. Chem. Eng. Data* 45 (4), 610–612.
- Ren, X., Zhao, Y., Deng, Q., Kang, J., Li, D., Wang, D., 2016. A relation of hydraulic conductivity—void ratio for soils based on Kozeny-Carman equation. *Eng. Geol.* 213, 89–97.
- Rinaldi, A.P., Rutqvist, J., 2013. Modeling of deep fracture zone opening and transient ground surface uplift at KB-502 CO₂ injection well, In Salah, Algeria. *Int. J. Greenhouse Gas Control* 12, 155–167.
- Rohmer, J., Pluymakers, A., Renard, F., 2016. Mechano-chemical interactions in sedimentary rocks in the context of CO₂ storage: weak acid, weak effects? *Earth-Sci. Rev.* 157, 86–110.
- Rutqvist, J., Tsang, C., 2002. A study of caprock hydromechanical changes associated with CO₂ injection into a brine formation. *Environ. Geol.* 42 (2), 296–305.
- Rutqvist, J., 2012. The geomechanics of CO₂ storage in deep sedimentary formations. *Geotech. Geol. Eng.* 30 (3), 525–551.
- Sánchez, M., Gens, A., Guimaraes, L. d. N., Olivella, S., 2005. A double structure generalized plasticity model for expansive materials. *Int. J. Numer. Anal. Methods Geomech.* 29 (8), 751–787.
- Sakurai, S., Ramakrishnan, T.S., Boyd, A., Mueller, N., Horovka, S.D., 2006. Monitoring saturation changes for CO₂ sequestration: petrophysical support for the Frio brine pilot experiment. *Petrophysics* 47 (6), 483–496.
- Santamarina, J.C., Klein, K.A., Fam, M.A., 2001. Soils and Waves. Wiley.
- Schaeff, H.T., Ilton, E.S., Qafoku, O., Martin, P.F., Felmy, A.R., Rosso, K.M.I., 2012. In situ XRD study of Ca²⁺ saturated montmorillonite (STX-1) exposed to anhydrous and wet supercritical carbon dioxide. *Int. J. Greenhouse Gas Control* 6, 220–229.
- Schlömer, S., Krooss, B.M., 1997. Experimental characterisation of the hydrocarbon sealing efficiency of cap rocks. *Mar. Petrol. Geol.* 14 (5), 565–580.
- Schowalter, T.T., 1979. Mechanics of secondary hydrocarbon migration and entrapment. *AAPG Bull.* 63 (5), 723–760.
- Shin, H., Santamarina, J.C., 2010. Fluid-driven fractures in uncemented sediments: underlying particle-level processes. *Earth Planet. Sci. Lett.* 299 (1–2), 180–189.
- Span, R., Wagner, W., 1996. A new equation of state for carbon dioxide covering the fluid region from the triple-point temperature to 1100 K at pressures up to 800 MPa. *J. Phys. Chem. Ref. Data* 25 (6), 1509–1596.
- Spycher, N., Pruess, K., Ennis-King, J., 2003. CO₂-H₂O mixtures in the geological sequestration of CO₂. I. Assessment and calculation of mutual solubilities from 12 to 100°C and up to 600 bar. *Geochim. Cosmochim. Acta* 67 (16), 3015–3031.
- Stumm, W., Morgan, J.J., 1996. Aquatic Chemistry: Chemical Equilibria and Rates in Natural Waters, 3rd ed. John Wiley & Sons, Inc, New York.
- Tanaka, Y., Yamachi, N., Matsumoto, S., Kaneko, S., Okabe, S., Shibuya, M., 2008. Thermodynamic and transport properties of CO₂, CO₂-O₂, and CO₂-H₂ mixtures at temperatures of 300–30,000-K and pressures of 0.1–10 MPa. *Electr. Eng. Jpn.* 163 (4), 18–29.
- Tonnet, N., Broseta, D., Mouronval, G., 2010. Evaluation of the petrophysical properties of a carbonate-rich caprock for CO₂ geological storage purposes. In: SPE EUROPEC-EAGE Annual Conference and Exhibition, Edited. Barcelona, Spain 14–17 June, 2010.
- Tonnet, N., Mouronval, G., Chiquet, P., Broseta, D., 2011. Petrophysical assessment of a carbonate-rich caprock for CO₂ geological storage purposes. *Energy Procedia* 4, 5422–5429.
- Watson, M.N., Zwingmann, N., Lemon, N.M., 2004. The Ladbroke Grove-Katnook carbon dioxide natural laboratory: a recent CO₂ accumulation in a lithic sandstone reservoir. *Energy* 29 (9–10), 1457–1466.
- Watson, M.N., Daniel, R.F., Tingate, P.R., Gibson-Poole, C.M., 2005. CO₂ related seal capacity enhancement in mudstones: evidence from the pine lodge natural CO₂ accumulation. In: Otway Basin, Australia, Paper Presented at International Conference on Greenhouse Gas Control Technologies. 7th: 2004: Vancouver, Canada.
- Wigley, M., Kampman, N., Dubacq, B., Bickle, M., 2012. Fluid-mineral reactions and trace metal mobilization in an exhumed natural CO₂ reservoir, Green River, Utah. *Geology* 40 (6), 555–558.
- Wollenweber, J., Alles, S., Busch, A., Krooss, B.M., Stanjek, H., Littke, R., 2010. Experimental investigation of the CO₂ sealing efficiency of caprocks. *Int. J. Greenhouse Gas Control* 4 (2), 231–241.
- Yokosoulian, L.E., Freiburg, J.T., Butler, S.K., Berger, P.M., Roy, W.R., 2013. Mineralogical alterations during laboratory-scale carbon sequestration experiments for the Illinois Basin. *Energy Procedia* 37, 5601–5611.
- Zhou, Q., Birkholzer, J.T., Mehnert, E., Lin, Y.F., Zhang, K., 2010. Modeling basin-and plume-scale processes of CO₂ storage for full-scale deployment. *Ground water* 48 (4), 494–514.